Journal of Heat and Mass Transfer Research

Journal homepage: https://jhmtr.semnan.ac.ir

Semnan University

Stagnation-Point Flow of a Walters' B Fluid Towards a Vertical Stretching Surface Embedded in a Porous Medium With Elastic-Deformation and Chemical Reaction

B.J. Akinbo *, **B.I. Olajuwon**

Department of Mathematics, Federal University of Agriculture, Abeokuta, Nigeria.

PAPER INFO

Paper history:
Received: 2020-11-03
Revised: 2022-06-03
Accepted: 2022-06-06

Keywords:
Chemical reaction;
Local weissenberg number;
Similarity variables;
Heat generation;
Homotopy analysis method (HAM).

ABSTRACT

In this paper, an analytical solution is presented for the stagnation-point flow of MHD viscous Walters' B fluid towards a vertical stretching surface with elastic-deformation, thermal radiation and chemical reaction. The higher non-linear ordinary differential equations for the heat and mass transfer are obtained from partial differential equations via similarity transformation techniques and solved by the modern analytical method. The behaviors of the various embedded parameter are addressed and the result justifies among others that the fluid exhibits Newtonian properties in the absence of local Weissenberg number. On the other hand, the presence of local Weissenberg number makes the model possess the Non-Newtonian properties with great industrial application such as plastic film, artificial fibers, and higher molecular-weight liquid used in industries and engineering field, while greater cooling problems commonly encountered in industries and engineering discipline for the cooling of the system or electronics components is observed with higher values of thermal buoyancy effect.

DOI: 10.22075/jhmtr.2022.21722.1313

1. Introduction

The boundary layer behavior of Newtonian fluid has gained significant attention in the years past due to its various scientific and engineering applications. Little among such applications is the boundary layer resistor in aerodynamics and fabrication of adhesive tapes. Singh et al. [1] worked on convective heat and mass transfer with the volumetric rate of heat generation/ absorption and the finding indicated among others that the rate of mass transfer is boosted with reverse phenomena with the rate of heat transfer over the enhancement on generation /absorption. Wu et al. [2] presented non-linear exact and asymptotic solutions of the Brinkman type of Navier–Stokes equation where the introduction of the Darcy term, makes the pressure field differs greatly from the classical stagnation-point flow. Akinbo and Olajuwon [3-5] investigated by means of Homotopy Analysis Method as well as Galerkin Weighted Residual Method the hydromagnetic flow via a vertical plate. The result revealed among others that the presence of convective heat parameter pave way for the penetration of thermal impact to the quiescent fluid.

Ellahi et al. [6] investigated the pressure-driven flow of aluminum oxide-water-based nanofluid with the combined impact of entropy generation and radiative electro-magnetohydrodynamics flow through a porous media via an asymmetric wavy channel where the residual errors are found to be minima at 20th order of iterations. Shehzad et al. [7] investigated internal energy loss due to entropy generation for non-Darcy Poiseuille flow of silver-water nanofluid where the enhancement in entropy was evident due to a rise in the pressure gradient.

Zeeshan et al. [8] observed decelerating nanofluid velocity via the enhancing modified magnetic field. However, the modern development in science and

* *Corresponding Author: B.J. Akinbo*
Email: akinbomaths@gmail.com

technology, finds Newtonian fluid not totally reliable while investigating higher molecular-weight liquid in the field, therefore, pioneered the existence of non-Newtonian fluid.

Shehzad et al. [9] examined electroosmotic flow of magnetohydrodynamics Power-law Al2O3-PVC nanofluid of Couette-Poiseuille flow model. It was reported that the flow and temperature exhibit the same enhanced reaction for improving the ratio of Helmholtz-Smoluchowski electro-osmotic velocity to maximum velocity as well as electro-osmotic field.

Mahapatra and Gupta [10] reported while investigating viscoelastic fluid towards a stretching surface that the flow near the stretching surface corresponds to an inviscid stagnation-point flow when the surface stretching velocity is equal to the free stream.

Hayat et al. [11] justified that the Newtonian fluid case can be retrieved by setting Weissenberg number to zero while investigating the heat transfer analysis in the flow of Walters' B fluid with a convective boundary condition.

Hakeem et al. [12] revealed the importance of radiation among others in cooling processes while investigating the effect of heat radiation in a Walters-liquid B fluid over a stretching sheet with non-uniform heat source/sink and elastic deformation.

Dhanalaxim [13] examined heat transfer in a viscoelastic fluid over a stretching sheet with frictional heating and work due to deformation.

Mishra et al. [14] reported that the presence of chemical reaction and lewis number diminish the temperature profile while studying heat and mass transfer on MHD Walters B' Nanofluid flow induced by a stretching porous surface.

Qayyum et al. [15] revealed that more heat is produced through the random motion of the fluid particles within the frame of large Brownian motion when examining the effect of a chemical reaction on MHD stagnation-point flow of Walters-B Nanofluid with Newtonian heat and mass condition.

Hayat et al. [16] examined the mixed convection in the stagnation-point flow adjacent to a vertical surface in a viscoelastic fluid.

Other Authors like Pillai et al. [17], Abel and Mahesha [18], Abel et al. [19,20] and Cortell [21] equally contributed to the latest development of the subject matter.

Keeping in mind the above-mentioned investigation, much attention has not been given to the combined impact of thermophysical parameters on the stagnation point flow of Walters' B fluid in the literature. On the account of this sequel, the aim of this study is to address the gap by extending the work in Makinde [22] to include the stagnation-point flow of a Walters' B fluid towards a vertical surface, embedded in a porous medium with elastic-deformation and chemical reaction. Walters' B fluid is a subclass of non-Newtonian fluid which is essential for polymer processing.

2. Mathematical Formulation

Consider the steady-state stagnation-point flow of a viscous incompressible hydromagnetic Walters' B fluid through a porous medium along with a vertical isothermal stretching sheet in the presence of volumetric rate of heat generation and uniform magnetic field B_0. In assumption, the fluid characteristics variation due to the temperature and chemical species concentration are limited to fluid density. Since the magnetic Reynolds number is noted to be very small in comparison with the applied magnetic field, therefore, the induced magnetic field is not taken into account. It is assumed that the velocity of the stretching sheet is $u_w(x) = ax$ and ambient fluid velocity $U_\infty(x) = cx$. The $x - axis$ is measured along with the plate and $y - axis$ is normal to it. The flow is being confined at $y > 0$ and potential fluid drops from $y - axis$ impinge on the surface, thereby making a division at stagnation point into two equal streams and the viscous flow heeds to the surface. The plate temperature (ambient temperature) and the surface concentration (ambient concentration) are respectively denoted by $T_w(> T_\infty)$ and $C_w(> C_\infty)$.

The equations for Walters' B fluid in tensorial form can be expressed (see Hayat et al. [11] and Nadeem *et al.* [23]) as;

$$S^* = 2\eta_0 - 2k_0\frac{\delta e}{\delta t} \tag{1}$$

Where e is the rate of the strain tensor, $\frac{\delta e}{\delta t}$ is the covariant differentiation of the rate of strain tensor in relation to the material motion, expressed as
$\frac{\delta e}{\delta t} = \frac{\partial e}{\partial t} + V.\nabla e - e\nabla V - (\nabla V)^T.e$,
while $\eta_0 = \int_0^\infty N(\tau)d\tau$ and $k_0 = \int_0^\infty \tau N(\tau)d\tau$ denote the limiting viscosity at low shear rates and short memory coefficient respectively with $N(\tau)$ being the distribution function with relaxation time τ. On the account of the short memory, the term involving $k_0 = \int_0^\infty \tau^n N(\tau)d\tau$ $(at\ n \geq 2)$ are neglected.

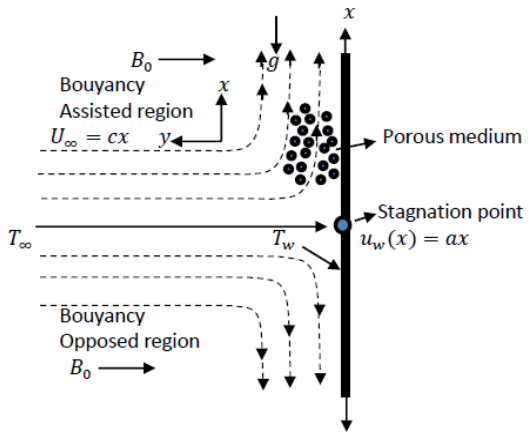

Figure 1. Flow configuration and coordinate system

Subject to the above expression with the appropriate approximation, the boundary layer equations for Walters' B fluid under this present investigation can be written as

$$\frac{\partial u}{\partial x}+\frac{\partial v}{\partial y}=0 \tag{2}$$

$$\begin{aligned} u\frac{\partial u}{\partial x}+v\frac{\partial u}{\partial y}&=U_\infty\frac{dU_\infty}{dx}+\nu\frac{\partial^2 u}{\partial y^2}\\ &-k_0\left[u\frac{\partial^3 u}{\partial x\partial y^2}+v\frac{\partial^3 u}{\partial y^3}+\frac{\partial u}{\partial x}\frac{\partial^2 u}{\partial y^2}-\frac{\partial u}{\partial y}\frac{\partial^2 u}{\partial x\partial y}\right]\\ &-\left(\frac{\sigma B_0^2 u}{\rho}+\frac{\nu}{K}\right)(u-U_\infty)+g\,\beta_T(T-T_\infty)\\ &+g\,\beta_c(C-C_\infty) \end{aligned} \tag{3}$$

$$\begin{aligned} u\frac{\partial T}{\partial x}+v\frac{\partial T}{\partial y}&=\alpha\frac{\partial^2 T}{\partial y^2}-\frac{\alpha}{k}\frac{\partial q_r}{\partial y}+\frac{\nu}{C_p}\left(\frac{\partial u}{\partial y}\right)^2\\ &-\frac{\delta k_0}{C_p}\left(\frac{\partial u}{\partial y}\right)\frac{\partial}{\partial y}\left[u\frac{\partial u}{\partial x}+v\frac{\partial u}{\partial y}\right]+Q_0(C-C_\infty) \end{aligned} \tag{4}$$

$$u\frac{\partial C}{\partial x}+v\frac{\partial C}{\partial y}=D\frac{\partial^2 C}{\partial y^2}-r(C-C_\infty) \tag{5}$$

Here, Q_0 is taken in line with Singh *et al*. [1] and Makinde [22], as the volumetric rate of heat generation and the suitable boundary condition are given as

$$u=u_w=ax, v=0, T=T_w, C=C_w \quad at \quad y=0 \tag{6}$$

$$u\to U_\infty=cx, \quad T\to T_\infty, \quad C\to C_\infty \qquad as \quad y\to\infty \tag{7}$$

where u and v as used above, stands for velocity components along x and y respectively, T denotes temperature while C stands for concentration. The radiative heat flux under the application of Roseland approximation is considered (Zeeshan *et al*. [24] and Alamri *et al*. [25]) as

$$q_r=\frac{-4\sigma^*}{3k^*}\frac{\partial T^4}{\partial y} \tag{8}$$

where σ^* (and k^*) connote the Sterfan-Boltzmann constant (and mean of the absorption coefficient). We take on the term T^4 as a linear function of temperature by subjecting T^4 to Taylor series about T_∞ and ignoring the higher-order terms gives

$$T^4\approx 4T_\infty^3T-3T_\infty^4 \tag{9}$$

Thus, applying (9) in (8), results in

$$\frac{\partial q_r}{\partial y}=-\frac{16\sigma^*T_\infty^3}{3k^*}\frac{\partial^2 T}{\partial y^2} \tag{10}$$

the continuity equation (2) is trivially satisfied with $u=\partial\psi/\partial y$ and $v=-\partial\psi/\partial x$ while the similarity solution of the governing equations are obtained by invoking (10) in (4) with the following transformation variables

$$\begin{aligned} &\eta=y\sqrt{\frac{a}{\nu}}, \quad \psi=x\sqrt{a\nu}f(\eta),\\ &\theta(\eta)=\frac{T-T_\infty}{T_w-T_\infty}, \quad \emptyset(\eta)=\frac{C-C_\infty}{C_w-C_\infty} \end{aligned} \tag{11}$$

Here, $\theta(\eta)$ represents dimensionless temperature, $\emptyset(\eta)$ body-forth dimensionless concentration while η stands for the independent similarity variable. Thus

$$\begin{aligned} &\frac{d^3f}{d\eta^3}+f(\eta)\frac{d^2f}{d\eta^2}-\left(\frac{df}{d\eta}\right)^2+\\ &We\left[\left(\frac{d^2f}{d\eta^2}\right)^2-2\frac{df}{d\eta}\frac{d^3f}{d\eta^3}+f(\eta)\frac{d^4f}{d\eta^4}\right]\\ &-(Mn+Ps)\left(\frac{df}{d\eta}-A\right)+A^2+\lambda_T\theta(\eta)\\ &+\lambda_M\emptyset(\eta)=0 \end{aligned} \tag{12}$$

$$\begin{aligned} &\left(1+\frac{4}{3}Ra\right)\frac{d^2\theta}{d\eta^2}+Prf(\eta)\frac{d\theta}{d\eta}+PrEc\left(\frac{d^2f}{d\eta^2}\right)^2\\ &-\delta WePrEc\left[\frac{df}{d\eta}\left(\frac{d^2f}{d\eta^2}\right)^2-f(\eta)\frac{d^2f}{d\eta^2}\frac{d^3f}{d\eta^3}\right]+Q\emptyset(\eta) \end{aligned} \tag{13}$$

$$\frac{d^2\emptyset}{d\eta^2}+Scf(\eta)\frac{d\emptyset}{d\eta}-RSc\emptyset(\eta)=0 \tag{14}$$

Satisfying the following boundary conditions

$$\begin{aligned} &\tfrac{df(\eta=0)}{d\eta}=1, \qquad f(\eta=0)=0,\\ &\theta(\eta=0)=1, \quad \emptyset(\eta=0)=1 \end{aligned} \tag{15}$$

$$\frac{\partial f(\eta\to\infty)}{\partial\eta}=A, \theta(\eta\to\infty)=0, \emptyset(\eta\to\infty)=0 \tag{16}$$

Where δ is the elastic deformation parameter, $R=\frac{r}{a}$ is the rate of chemical reaction, $Mn=\frac{\sigma B_0^2}{\rho a}$ is the magnetic field, $We=\frac{ak_0}{\nu}$ is the local Weissenberg Number, $\lambda_T=\frac{Gr_x}{(Re_x)^2}$ is the thermal buoyancy parameter, $\lambda_M=\frac{Gc_x}{(Re_x)^2}$ is the mass buoyancy parameter, $Gr_x=\frac{g\beta_T(T_w-T_\infty)x^3}{\nu^2}$ is the thermal Grashof Number, $Gc_x=\frac{g\beta_C(C_{w-}-C_\infty)x^3}{\nu^2}$ is the solutal Grashof Number, $Re_x=\frac{u(x)}{\nu}$ is the Reynolds Number, $Pr=\frac{\nu\rho Cp}{k}$ is the Prandtl number, $Sc=\frac{\nu}{D}$ is the Schmidt number, $Ps=\frac{\nu}{Ka}$ is the porosity parameter, $Ra=\frac{4\sigma^*T_\infty^3}{k^*k}$ is the radiation parameter, $Ec=\frac{u_w^2}{C_p(T_w-T_\infty)}$ is the Eckert number, $Q=\frac{Q_0(C_w-C_\infty)\nu}{a(T_w-T_\infty)\alpha}$ denotes internal heat generation/Absorption and A is the ratio rate.

Owing to the engineering application of the study, the expression for skin friction coefficient, local Nusselt number, and Local Sherwood number are respectively put into consideration as

$$C_f = \frac{2\tau_w}{\rho u_w^2}, \quad Nu = \frac{xq_w}{k(T_w - T_\infty)} \quad and \quad Sh = \frac{xq_m}{D(C_w - C_\infty)} \tag{17}$$

Here, τ_w typifies the shear stress on the plate, q_w body-forth surface heat while q_m denotes the surface mass.

$$\tau_w = \left[\mu\frac{\partial u}{\partial y} - k_0\left(u\frac{\partial^2 u}{\partial x \partial y} + v\frac{\partial^2 u}{\partial y^2} + 2\frac{\partial u}{\partial x}\frac{\partial v}{\partial y}\right)\right]_{y=0}$$

$$q_w = \left[-k\frac{\partial T}{\partial y}\right]_{y=0} = \left[-\frac{4\sigma}{3k^*}\frac{\partial T^4}{\partial y}\right]_{y=0}, \tag{18}$$

$$q_m = \left[-D\frac{\partial C}{\partial y}\right]_{y=0} = 0$$

Considering equations (17) and (18) with (11) result in

$$Re_x^{\frac{1}{2}} C_f = (1 - We) f''(0),$$

$$Re_x^{-\frac{1}{2}} Nu = -\left(1 + \frac{4}{3}Ra\right)\theta'(0), \tag{19}$$

$$Re_x^{-\frac{1}{2}} Sh = -\emptyset'(0)$$

3. Method of Solution

Homotopy Analysis Method is adopted over others such as Variation Iterations Method, Adomial Decomposition and Differential Transformation Method, e.t.c, being a modern method and very efficient in solving both bounded and unbounded domain of nonlinear differential equations. Subject to the rule of solution and boundary conditions (15) and (16), the initial guess

$$f_0(\eta) = A * \eta + (1 - A)[1 - exp(-\eta)], \quad \theta_0(\eta) = exp(-\eta), \quad \emptyset_0(\eta) = exp(-\eta) \tag{20}$$

and the auxiliary linear operations L_f, L_θ, and $L_\emptyset$ which are respectively taken as;

$$L_f[f(\eta;r)] = \frac{\partial^3 f(\eta;r)}{\partial \eta^3} - \frac{\partial f(\eta;r)}{\partial \eta}, \quad L_\theta[\theta(\eta;r)] = \frac{\partial^2 \theta(\eta;r)}{\partial \eta^2} - \theta(\eta;r), \quad L_\emptyset[(\eta;r)] = \frac{\partial^2 \emptyset(\eta;r)}{\partial \eta^2} - \emptyset(\eta;r) \tag{21}$$

satisfy the following properties

$$L_f[C_1 + C_2\, exp(\eta) + C_3\, exp(-\eta)] = 0, \quad L_\theta[C_4 + C_5\, exp(-\eta)] = 0, \quad L_\emptyset[C_6 + C_7\, exp(-\eta)] = 0 \tag{22}$$

where $C_1, C_2, \ldots, C_7$ stand for constants.

3.1. Zero-Order Deformation

$$(1 - r)L_f[f(\eta;r) - f_0(\eta)] = r\hbar_f H_f(\eta) N_f[f(\eta;r), \theta(\eta;r), \emptyset(\eta;r)] \tag{23}$$

$$(1 - r)L_\theta[f(\eta;r) - \theta_0(\eta)] = r\hbar_\theta H_\theta(\eta) N_\theta[f(\eta;r), \theta(\eta;r), \emptyset(\eta;r)] \tag{24}$$

$$(1 - r)L_\emptyset[f(\eta;r) - \emptyset_0(\eta)] = r\hbar_\emptyset H_\emptyset(\eta) N_\emptyset[f(\eta;r), \emptyset(\eta;r)] \tag{25}$$

here, $\hbar \neq 0$ and $H \neq 0$ denotes the auxiliary functions and $r \in [0,1]$ represent embedded parameter, under the conditions stated below.

$$\frac{\partial f(\eta;r)}{\partial \eta}\Big|_{\eta=0} = 1, \quad f(\eta = 0, r) = 0, \quad \theta(\eta = 0, r) = 1, \quad \emptyset(\eta = 0, r) = 1 \tag{26}$$

$$\frac{\partial f(\eta;r)}{\partial \eta}\Big|_{\eta\to\infty} = A, \quad \theta(\eta \to \infty, r) = 0, \quad \emptyset(\eta \to \infty, r) = 0 \tag{27}$$

The nonlinear operators N_f, N_θ, and $N_\emptyset$ are respectively expressed as

$$N_f[f(\eta;r), \theta(\eta;r), \emptyset(\eta;r)] = \frac{\partial^3 f}{\partial \eta^3} + f(\eta)\frac{\partial^2 f}{\partial \eta^2} - \left(\frac{\partial f}{\partial \eta}\right)^2 + \beta\left[\left(\frac{\partial^2 f}{\partial \eta^2}\right)^2 - 2\frac{\partial f}{\partial \eta}\frac{\partial^3 f}{\partial \eta^3} + f(\eta)\frac{\partial^4 f}{\partial \eta^4}\right] - (Mn + Ps)\left(\frac{\partial f}{\partial \eta} - A\right) + A^2 + \lambda_T \theta(\eta) + \lambda_M \emptyset(\eta) = 0 \tag{28}$$

$$N_\theta[f(\eta;r), \theta(\eta;r)] = \left(1 + \frac{4}{3}Ra\right)\frac{\partial^2 \theta}{\partial \eta^2} + Prf(\eta)\frac{\partial \theta}{\partial \eta} + PrEc\left(\frac{\partial^2 f}{\partial \eta^2}\right)^2 - \delta WePrEc\left[\frac{\partial f}{\partial \eta}\left(\frac{\partial^2 f}{\partial \eta^2}\right)^2 - f(\eta)\frac{\partial^2 f}{\partial \eta^2}\frac{\partial^3 f}{\partial \eta^3}\right] + Q\emptyset(\eta) \tag{29}$$

$$N_\emptyset[f(\eta;r), \emptyset(\eta;r)] = \frac{\partial^2 \emptyset}{\partial \eta^2} + Scf(\eta)\frac{\partial \emptyset}{\partial \eta} - RSc\emptyset(\eta) = 0 \tag{30}$$

Introducing $r = 0$ and $r = 1$, we have

$$f(\eta;0) = f_0(\eta), \quad \theta(\eta;0) = \theta_0(\eta), \quad \emptyset(\eta;0) = \emptyset\_0\ (\eta) \tag{31}$$

$$f(\eta;1) = f(\eta), \theta(\eta;1) = \theta(\eta), \emptyset(\eta;1) = \emptyset(\eta) \tag{32}$$

As r rise from zero to one, the function $f(\eta;r), \theta(\eta;r)$ and $\emptyset(\eta;r)$ approaches $f_0(\eta), \theta_0(\eta)$ and $\emptyset_0(\eta)$ to be solutions $f(\eta)$, $\theta(\eta)$ and $\emptyset(\eta)$. In Taylor series, the expansion for $f(\eta;r), \theta(\eta;r)$ and $\emptyset(\eta;r)$ are respectively consider as

$$f(\eta;r)=f_0(\eta)+\sum_{m=1}^{\infty}f_m(\eta)r^m,$$
$$\theta(\eta;r)=\theta_0(\eta)+\sum_{m=1}^{\infty}\theta_m(\eta)r^m$$
$$\emptyset(\eta;r)=\emptyset_0(\eta)+\sum_{m=1}^{\infty}\emptyset_m(\eta)r^m \quad (33)$$
$$f_m(\eta)=\frac{1}{m!}\frac{\partial^m f(\eta;r)}{\partial\eta^m}\Big|_{r=0},$$
$$f_m(\eta)=\frac{1}{m!}\frac{\partial^m \theta(\eta;r)}{\partial\theta^m}\Big|_{r=0},$$
$$f_m(\eta)=\frac{1}{m!}\frac{\partial^m \emptyset(\eta;r)}{\partial\emptyset^m}\Big|_{r=0}$$

the convergence of the equation (33) concurred with the auxiliary parameter $\hbar$. supposing $\hbar$ is taken in such a way that the series (33) converge at $r=1$, then

$$f(\eta)=f_0(\eta)+\sum_{m=1}^{\infty}f_m(\eta),$$
$$\theta(\eta)=\theta_0(\eta)+\sum_{m=1}^{\infty}\theta_m(\eta), \quad (34)$$
$$\emptyset(\eta)=\emptyset_0(\eta)+\sum_{m=1}^{\infty}\emptyset_m(\eta)$$

The mth-order deformation are expressed as

$$L_f[f_m(\eta)-\chi_m f_{m-1}(\eta)]=\hbar R_m^f(\eta),$$
$$L_\theta[\theta_m(\eta)-\chi_m\theta_{m-1}(\eta)]=\hbar R_m^\theta(\eta) \quad (35)$$
$$L_\emptyset[\emptyset_m(\eta)-\chi_m\emptyset_{m-1}(\eta)]=\hbar R_m^\emptyset(\eta)$$

$$\frac{\partial f(\eta)}{\partial\eta}\Big|_{\eta=0}=0, f(\eta=0)=0,$$
$$\frac{\partial f(\eta)}{\partial\eta}\Big|_{\eta\to\infty}=0, \quad (36)$$
$$\theta(\eta=0)=0, \qquad \emptyset(\eta=0)=0,$$
$$\theta(\eta\to\infty)=0, \qquad \emptyset(\eta\to\infty)=0$$

$$R_m^f(\eta)=\frac{d^3f_{m-1}(\eta)}{d\eta^3}+\sum_{n=0}^{m-1}f_n(\eta)\frac{d^2f_{m-1-n}(\eta)}{d\eta^2}$$
$$-\sum_{n=0}^{m-1}\frac{df_n(\eta)}{d\eta}\frac{df_{m-1-n}(\eta)}{d\eta}$$
$$-\beta\left[2\sum_{n=0}^{m-1}\frac{df_n(\eta)}{d\eta}\frac{d^2f_{m-1-n}(\eta)}{d\eta^2}-\sum_{n=0}^{m-1}f_n(\eta)\frac{d^4f_{m-1-n}(\eta)}{d\eta^4}-\sum_{n=0}^{m-1}\frac{d^2f_n(\eta)}{d\eta^2}\frac{d^2f_{m-1-n}(\eta)}{d\eta^2}\right] \quad (37)$$
$$-(Mn+Ps)\frac{df_{m-1}(\eta)}{d\eta}+\lambda_T\theta_{m-1}+\lambda_M\emptyset_{m-1}(\eta)$$

$$R_m^\theta(\eta)=\left(1+\frac{4}{3}Ra\right)\frac{d^2\theta_{m-1}(\eta)}{d\eta^2}$$
$$+Pr\sum_{n=0}^{m-1}f_n(\eta)\frac{d\theta_{m-1-n}(\eta)}{d\eta}+Q\emptyset_{m-1}(\eta)$$
$$+PrEc\sum_{n=0}^{m-1}f_n(\eta)\frac{d^2f_n(\eta)}{d\eta^2}\frac{d^2f_{m-1-n}(\eta)}{d\eta^2} \quad (38)$$
$$-\delta WePrEc\left[\sum_{l=0}^{m-1}\frac{d^2f_{m-1-l}(\eta)}{d\eta^2}\left(\sum_{j=0}^{l}\frac{d^2f_{l-j}(\eta)}{d\eta^2}\frac{df_j(\eta)}{d\eta}\right)-\sum_{l=0}^{m-1}f_{m-1-l}(\eta)\left(\sum_{j=0}^{l}\frac{d^2f_{l-j}(\eta)}{d\eta^2}\frac{d^3f_j(\eta)}{d\eta^3}\right)\right]$$

$$R_m^\emptyset(\eta)=\frac{d^2\emptyset_{m-1}(\eta)}{d\eta^2}-RSc\emptyset_{m-1}(\eta)$$
$$+Sc\sum_{n=0}^{m-1}f_{m-1-n}(\eta)\frac{df_n(\eta)}{d\eta} \quad (39)$$

and $\chi_m=0 \ \ for \ \ m\le 1, \quad \chi_m=1 \ \ for \ \ m>1$

Therefore, the general solutions of equations (35-36) are

$$f_m(\eta)=f_m^*(\eta)+C_1+C_2\,exp(-\eta)+C_3\,exp(\eta) \quad (40)$$

$$\theta_m(\eta)=\theta_m^*(\eta)+C_4+C_5\,exp(\eta) \quad (41)$$

$$\emptyset_m(\eta)=\emptyset_m^*(\eta)+C_6+C_7\,exp(\eta) \quad (42)$$

3.2. Convergence of the HAM Solution

Keeping in mind the Liao [26] and Akinbo and Olajuwon [27-28] suggestions, the non-zero auxiliary parameters $\hbar_f$, $\hbar_\theta$ and $\hbar_\emptyset$ significantly help in adjusting the convergence region of the series solution. On the account of the following embedded parameters $Ra=0.7$, $Ec=1.0$, $We=0.1$, $Mn=0.1$, $Ps=0.1$, $\lambda_T=0.1$, $\lambda_M=0.1$, $Pr=0.72$, $Sc=0.62$, $\delta=1.0$, $A=0.2$, $R=0.1$ and $Q=0.1$, the acceptable values of $\hbar_f$, $\hbar_\theta$ and $\hbar_\emptyset$ are captured at a region where $\hbar-$curve becomes parallel, such as $-0.7\le\hbar_f\le-0.1$, $-1.3\le\hbar_\theta\le-0.1$ and $-1.3\le\hbar_\emptyset\le-0.2$ (See Fig. 2).

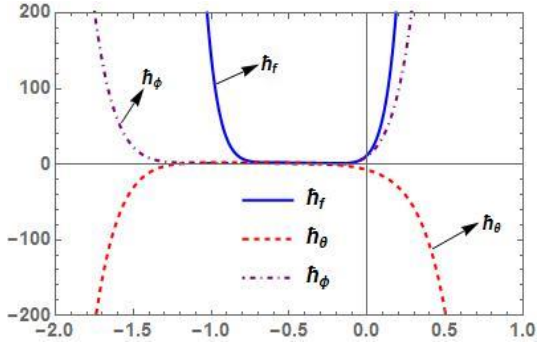

Figure 2. $\hbar_f$, $\hbar_\theta$, $\hbar_\emptyset$-curves for f′′(0), θ′(0) and ∅′(0) respectively

Table 1. Convergence of solution with the CPU time

Order of Approximations	CPU time	$f''(0)$	$-\theta'(0)$	$-\emptyset'(0)$
4	13.20	-1.4312	0.1097	0.5044
10	133.76	-1.4566	0.0592	0.4959
12	227.49	-1.4569	0.0567	0.4960
14	366.97	-1.4570	0.0556	0.4961
16	613.84	-1.4570	0.0550	0.4961
18	1988.01	-1.4570	0.0548	0.4962
20	1529.74	-1.4570	0.0547	0.4962
22	2243.73	-1.4570	0.0546	0.4962
24	3205.39	-1.4570	0.0546	0.4962

Table 1 reveals the convergence of the iterations with the unbounded domain. As presented in the table, the momentum equation demonstrated a quick convergence at 14th-order of iterations while concentration and energy equations meet the far-field boundary conditions at 18th-order and 22th-order of iterations respectively.

Table 2 presents individual errors of the series solution via Homotopy Analysis Method with the indicated parameters. Clearly from the table, as the order of approximation increases, the residual errors reduced.

4. Validation of the study

This work is first compared under the domain adopted in Singh *et al*. [1] by setting $We = 0$, $Ec = 0$, $R = 0$, $Mn = 0$ and $\delta = 0$ as well as Makinde [22] by setting $We = 0$, $Ec = 0$, $R = 0$ and $\delta = 0$. The results demonstrated a perfect agreement with each other as shown in table 3.

Table 2. Residual errors of the series solution

m	Er_m^f	Er_m^θ	$Er_m^\emptyset$
4	1.806×10^{-4}	2.606×10^{-4}	2.567×10^{-6}
10	1.889×10^{-7}	1.93×10^{-6}	2.174×10^{-9}
12	3.406×10^{-8}	4.283×10^{-7}	7.985×10^{-10}
14	3.551×10^{-9}	9.228×10^{-8}	2.345×10^{-10}
16	1.238×10^{-9}	1.901×10^{-8}	1.844×10^{-10}
18	2.016×10^{-10}	3.706×10^{-9}	1.015×10^{-11}
20	4.684×10^{-10}	9.308×10^{-10}	8.333×10^{-11}
22	1.899×10^{-10}	3.435×10^{-10}	9.734×10^{-11}
24	1.972×10^{-11}	4.127×10^{-10}	1.818×10^{-12}

Table 3. Comparison of the result with Singh *et al*. [1] and Makinde [22]

Q	$f''(0)$ [1]	$-\theta'(0)$ [1]	$-\emptyset'(0)$ [1]	$f''(0)$ [22]	$-\theta'(0)$ [22]	$-\emptyset'(0)$ [22]	$f''(0)$ Present	$-\theta'(0)$ Present	$-\emptyset'(0)$ Present
-1	1.8444	1.3908	0.4631	1.844462	1.390856	0.463174	1.844459	1.390845	0.463168
0	1.9995	0.6392	0.4789	1.999553	0.639244	0.478964	1.999546	0.639238	0.478955
1	2.1342	-0.0730	0.4917	2.134287	-0.073040	0.491749	2.134277	-0.073036	0.491736

Table 4. Numerical values of the local Skin-friction coefficient, Local Nusselt number, and Local Sherwood number/Validation via Galerkin weighted residual method(GWRM) at $A = 0.2$

												HAM			GWRM		
We	Mn	λ_T	λ_M	Pr	Sc	Ra	Ec	Q	R	δ	Ps	$Re_x^{\frac{1}{2}}C_f$	$Re_x^{-\frac{1}{2}}Nu$	$Re_x^{-\frac{1}{2}}Sh$	$Re_x^{\frac{1}{2}}C_f$	$Re_x^{-\frac{1}{2}}Nu$	$Re_x^{-\frac{1}{2}}Sh$
0.1	0.1	0.1	0.1	0.72	0.62	0.7	1.0	0.1	0.1	1.0	0.1	−0.824082	0.352957	0.535467	−0.824076	0.352955	0.535458
0.3												−0.756115	0.344329	0.520938	−0.756120	0.344326	0.520926
0.5												−0.689258	0.324723	0.499130	−0.689249	0.324719	0.499129
	1.0											−1.092921	0.234870	0.511914	−1.092915	0.234867	0.511912
	2.0											−1.333624	0.134420	0.494694	−1.333622	0.134419	0.494687
		1.0										−0.283947	0.611390	0.601486	−0.283938	0.611386	0.601479
		2.0										0.283302	0.698849	0.651050	0.283290	0.698846	0.651046
			1.0									−0.362700	0.540106	0.583043	−0.362681	0.540112	0.583041
			2.0									0.127342	0.621100	0.621915	0.127338	0.621101	0.621920
				3.0								−0.840791	0.664945	0.529531	−0.840787	0.664939	0.529528
				7.1								−0.848918	0.735177	0.527523	−0.848916	0.735175	0.527520
					0.24							−0.811240	0.314469	0.310631	−0.811236	0.314466	0.310626
					0.78							−0.827473	0.360216	0.610984	−0.827465	0.360214	0.610982
						2.0						−0.820059	0.581937	0.537417	−0.820048	0.581935	0.537415
						3.0						−0.818199	0.738754	0.538306	−0.818195	0.738749	0.538314
							2.0					−0.822501	0.148371	0.535896	−0.822500	0.148366	0.535888
							4.0					−0.818961	−0.254804	0.536739	−0.818957	−0.254801	0.536736
								0.5				−0.817206	−0.063367	0.537653	−0.817205	−0.063358	0.537648
								1.0				−0.808664	−0.576160	0.540218	−0.808658	−0.576159	0.540215
									0.5			−0.829733	0.364052	0.734193	−0.829725	0.364045	0.734185
									1.0			−0.833985	0.372047	0.924503	−0.833983	0.372038	0.924501
										5.0		−0.825254	0.454292	0.535233	−0.825246	0.454290	0.535227
										10		−0.826457	0.581634	0.534937	−0.826449	0.581632	0.534935
											1.0	−1.092921	0.234870	0.511914	−1.092920	0.234869	0.511911
											2.0	−1.333624	0.134420	0.494694	−1.333622	0.134417	0.494689

5. Discussion of Results

This section presents the dynamics of the different patients for a better understanding of the study. The parameters are discussed by keeping $Ra = 0.7, Ec = 1, We = 0.1, Mn = 0.1, Ps = 0.1, \lambda_T = 0.1, \lambda_M = 0.1, Pr = 0.72, Sc = 0.62, \delta = 1.0, A = 0.2, R = 0.1$ and $Q = 0.1$, fixed for each varying parameter. It is noticed from table 4 that almost all the values of the local skin-friction $Re_x^{\frac{1}{2}} C_f$ are negatives. This pioneer drags forces on the plate and impedes the flow. However, the local Nusselt number $Re_x^{-\frac{1}{2}} Nu$ and Sherwood number $Re_x^{-\frac{1}{2}} Sh$ improves for large values of Radiation parameter (Ra), thermal and mass buoyancy parameter (λ_T, λ_M). This in turns, strengthen the surface heat and mass transfer with the opposite results as Weissenberg number (We) and Magnetic Parameter (Mn) varied. Moreover, It is also observed from the table that the rate of heat transfer is strengthened at higher values of Prandtl number (Pr), Radiation parameter (Ra) and elastic deformation (δ) while the presence of a chemical reaction $(R) > 0$ and $(Sc) > 0$ magnifies the rate of mass transfer. The results through Homotopy Analysis Method agreed when compared with Galerkin Weighted Residual Method (see table 4).

The impact of magnetic interaction $Mn > 0$ is reported in Fig. (3-4). The introduction of a transverse magnetic field in an electrically conducting fluid pioneer a resistive force called Lorentz force which inturns slow down the motion of the fluid and lower its layer thickness. However, the presence of Lorentz force gives rise to more frictional heating which ultimately strengthens the fluid temperature and its layer thickness.

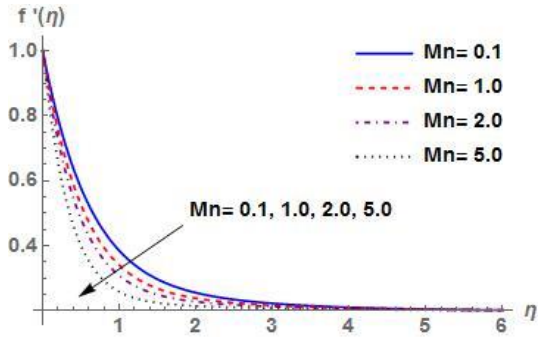

Figure 3. Reaction of Mn on velocity f′(η)

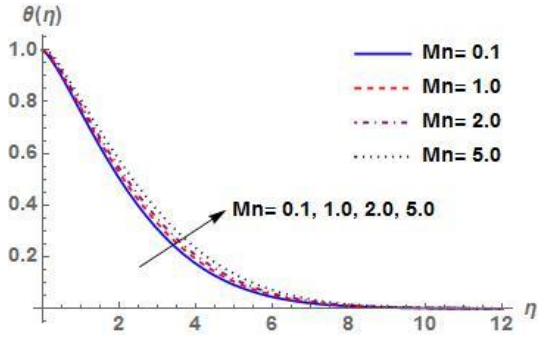

Figure 4. Reaction of Mn on temperature $\theta(\eta)$

Fig. (5-6) are plotted to justify the behavior of thermal buoyancy parameter (λ_T) on velocity and temperature profiles while Fig. (7-8) reveals the effect of mass buoyancy parameter (λ_M) on velocity and concentration profiles. It is observed that the fluid motion is magnified for higher values of (λ_T, λ_M) (see Fig. 5 and Fig. 7) which inturns magnified its layer thickness with the opposite influence on temperature and concentration profiles respectively (see Fig. 6 and Fig. 8). It is noteworthy that $(\lambda_T, \lambda_M) > 0$ corresponds to cooling problem and greater concentration is noticed at the plate surface in comparison with the free stream concentration.

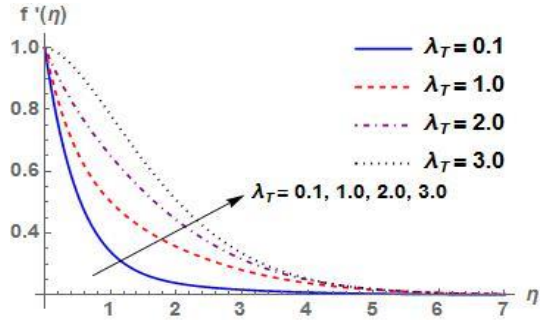

Figure 5. Reaction of λ_T on velocity $f'(\eta)$

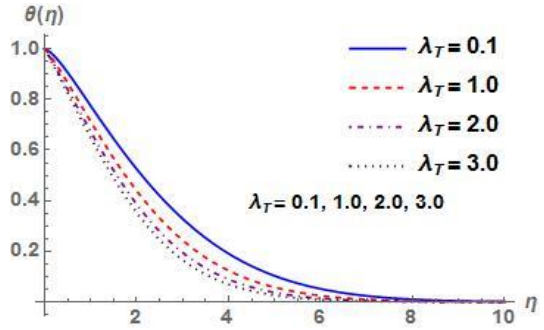

Figure 6. Reaction of of λ_T on temperature $\theta(\eta)$

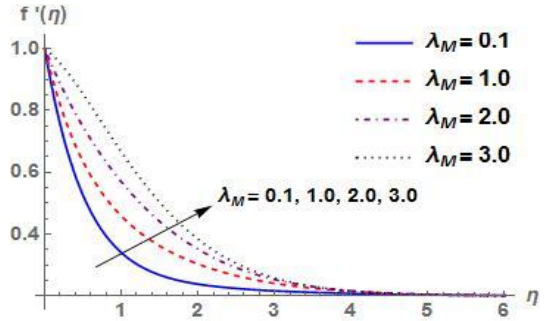

Figure 7. Reaction of λ_M on velocity f′(η)

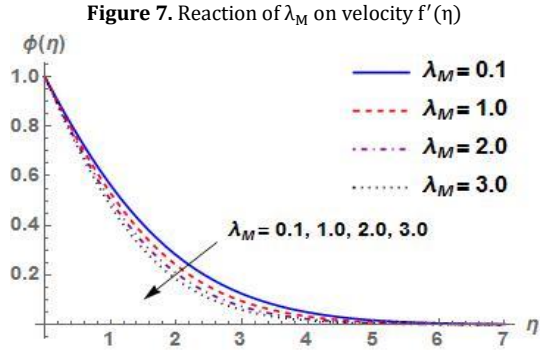

Figure 8. Reaction of λ_M on concentration $\emptyset(\eta)$

Fig. (9-10) analyzes the behaviors of local Weissenberg number (We) on velocity and temperature profiles. Large values of We consequently improve the viscoelasticity through the tensile stress and depress the velocity of the fluid and its layer thickness. However, more energy is stirred-up within the boundary which thusly increases the thermal layer thickness, owing to an increase in temperature of the fluid.

Fig. 11 elucidates the behavior of Prandtl number (Pr) on dimensionless temperature. Prandtl number is inversely proportional to thermal conductivity. Higher values of Pr correspond to polymers since the polymer possesses lower thermal diffusivities (Shahid *et al.* [29]), thereby pioneering the falling of the temperature distribution across the boundary layer and lowering its layer thickness. Fig. 12 illustrates the influence of Schmidt number (Sc) on the concentration profile. The low molecular diffusivity brings about an increase in Sc that consequently diminishes the diffusion properties of the fluid which consequently decreases the concentration profile, this, in turn, result in a thinning concentration boundary layer.

Fig. 13 presents the thermal boundary layer, being strengthened, owing to an elevation in temperature profile for higher values of Eckert number (Ec) in the presence of elastic deformation that occurs as a result of energy stored in the liquid due to the frictional heating (see ref. [12]). However, the presence of elastic deformation (δ) displayed a very little decreasing negligible effect on temperature profile (see Fig. 14).

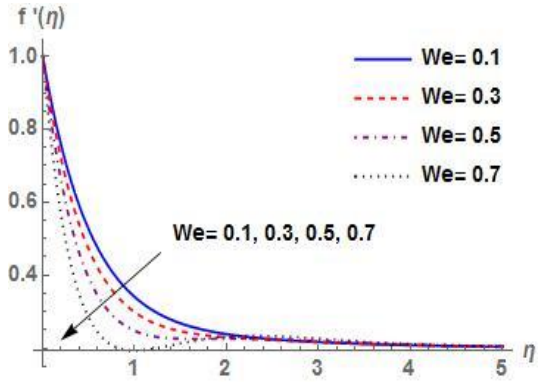

Figure 9. Reaction of We on velocity f′(η)

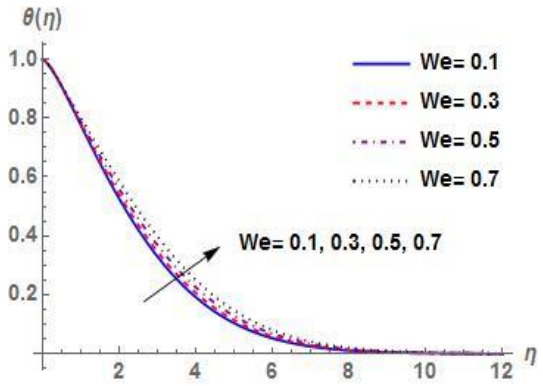

Figure 10. Reaction of We on temperature $\theta(\eta)$

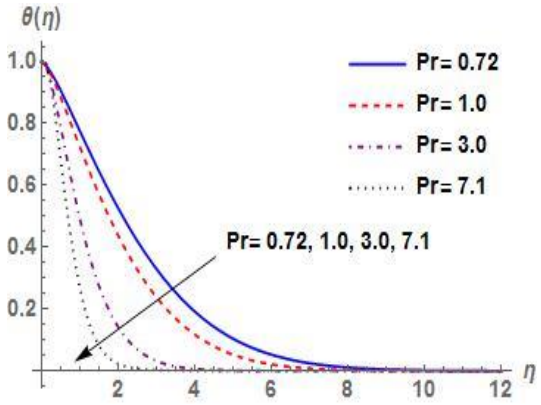

Figure 11. Reaction of Pr on temperature $\theta(\eta)$

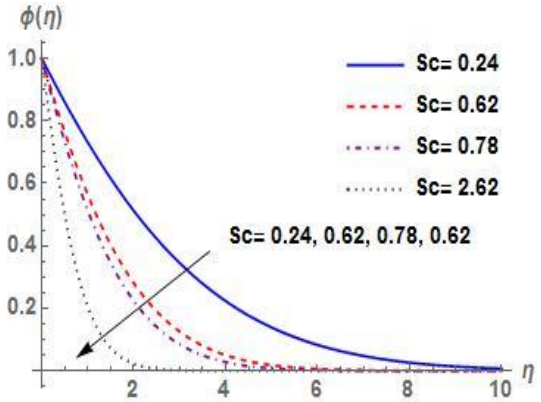

Figure 12. Reaction of Sc on concentration $\emptyset(\eta)$

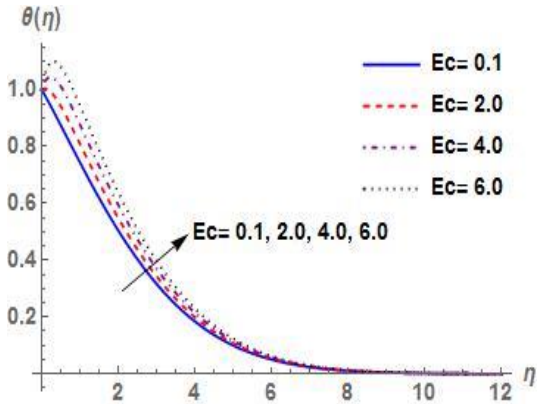

Figure 13. Reaction of Ec on temperature $\theta(\eta)$

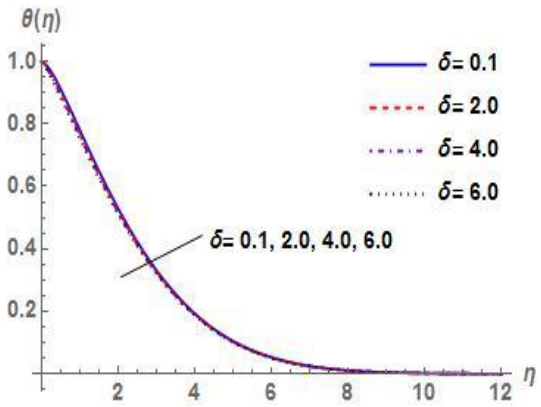

Figure 14. Reaction of δ on temperature $\theta(\eta)$

The presence of Radiation parameter $(Ra) > 0$ pioneer heat from the radiation processes in the operating fluid, which consequently magnified the temperature field as well as thermal layer thickness (see Fig 15).

Fig. 16 depicts the behaviors of heat source parameter (Q) on the temperature profile. As expected, the temperature profile overshoot for higher values of Q. This in turn enhances the thermal layer thickness and enables the thermal effect to fall deeper into the quiescent fluid.

Fig. (17-18) are presented to describe the behavior of the porosity parameter (Ps) on dimensionless velocity as well as temperature fields. Increase in the magnitude of Ps demonstrated high porosity in the medium, which in turn slows down the motion of the fluid and reduces its layer thickness. However, the reverse phenomenon is observed in the temperature profile as a slow movement of the fluid particles generates more heat that consequently strengthens the thermal boundary layer thickness.

Various values of chemical reaction (R) as reported in Fig. 19 decline the concentration profile which results in a decrease in its layer thickness. Here, $R > 0$ decays concentration buoyancy impact and decreases concentration field. Fig. 20 captures the behavior of ratio parameter (A) on velocity field. Moreover, the motion of the fluid and the momentum layer are boosted at different values of A but portrayed opposite behavior at $A < 1$ and $A > 1$. However, at $A = 1$, the fluid and the stretching velocity are one, which inturns justify that the boundary layer is not in existence.

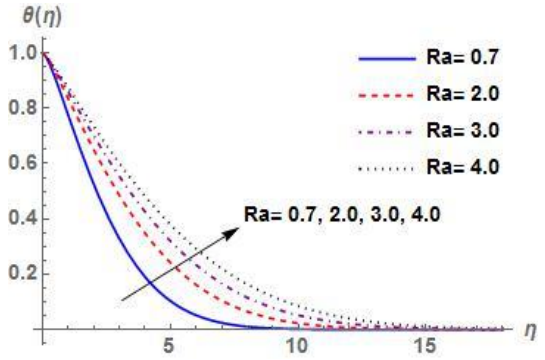

Figure 15. Reaction of Ra on temperature $\theta(\eta)$

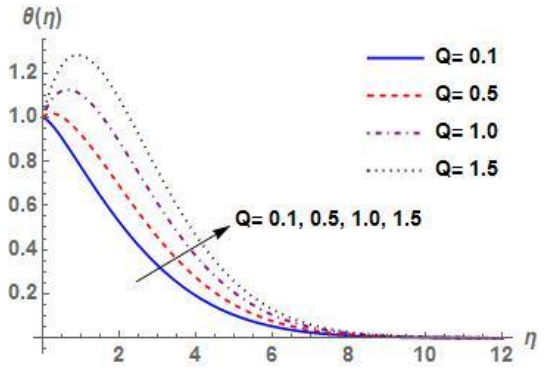

Figure 16. Reaction of Q on temperature $\theta(\eta)$

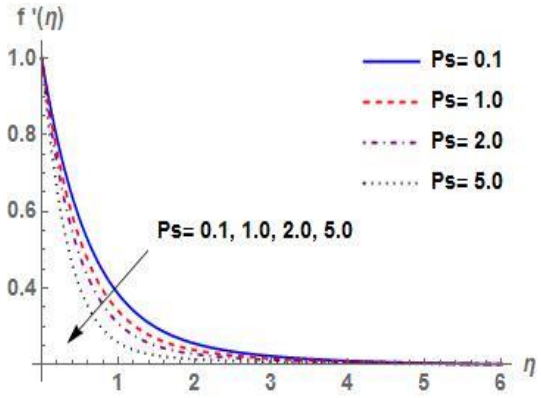

Figure 17. Reaction of Ps on velocity $f'(\eta)$

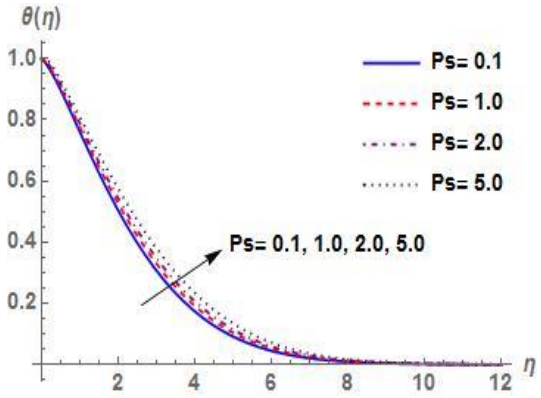

Figure 18. Reaction of of P_s on temperature $\theta(\eta)$

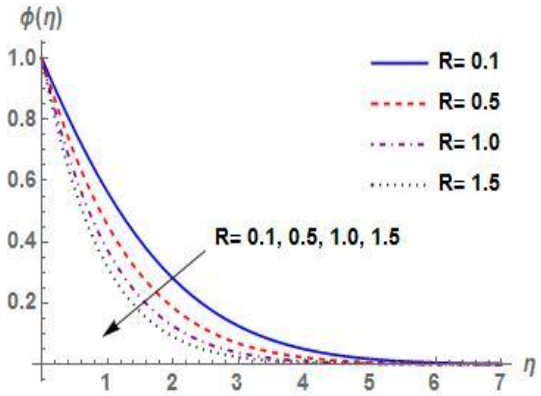

Figure 19. Reaction of R on concentration $\emptyset(\eta)$

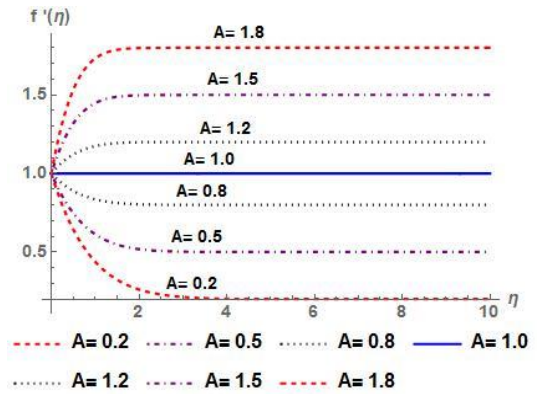

Figure 20. Reaction of A on velocity $f'(\eta)$

Conclusion

In this work, HAM is adopted at the *20th-order* of approximation to solve the governing equations corresponding to Momentum, Energy, and Concentration equations, describing the stagnation-point flow of a Walters' B fluid towards a vertical surface embedded in a porous medium with elastic-deformation and chemical reaction. The reason for this *order* of approximation is to meet the far-field conditions. The parameters encountered are discussed accordingly through graphs and tables and the following conclusions are drawn.

- Higher values of chemical reaction deteriorate the concentration buoyancy effect and lower the concentration boundary layer thickness.
- The temperature distribution is strengthened due to the slow movement of the fluid particles with the interaction of the porosity parameter and enhances the thermal boundary layer thickness.
- The fluid exhibits Newtonian properties in the absence of local Weissenberg number, while the presence of Weissenberg number pioneers viscoelasticity through the tensile stress and depresses the momentum boundary layer thickness. The non-Newtonian fluid has great industrial applications among which are plastic film, artificial fibers, and higher molecular-weight liquid used in the Science discipline.
- The fluid temperature gain more strength for large values of viscous dissipation as heat energy is stored in the liquid due to the frictional heating
- Higher values of thermal buoyancy parameter contribute to the cooling problem while mass buoyancy parameter shows a greater concentration at the plate surface than free stream concentration. The cooling process plays an important role in the Science and Engineering disciplines such as the cooling of electronic components.

Nomenclature

Mn	Magnetic field
We	Local Weissenberg number
λ_T	Thermal buoyancy parameter
λ_M	Mass buoyancy parameter
Pr	Prandtl number
Sc	Schmidt number
Ps	permeability parameter
Ra	Radiation parameter
Ec	Eckert number
Q	Internal heat generation/Absoption
U_∞	Ambient velocity $[ms^{-\prime}]$
u_w	Stretching velocity $[ms^{-\prime}]$
α	Thermal diffusivity $[m^2.s^{-\prime}]$
β_c	Concentration expansion coefficient $[m^3kg^{-\prime}]$
η	Similarity variable
θ	Dimensionless temperature
v	Kinematic viscosity $[m^2.s^{-\prime}]$
ψ	Stream Function $[m^2.s^{-\prime}]$
ρ	Density $[kgm^{-3}]$
q_r	Radiation heat flux [W/m^2]
C_p	Specific heat at constant pressure $[J.kg^{-\prime}.K^{-\prime}$
β_T	Temperature expansion coefficient $[1/k]$
g	Acceleration due to gravity $[sm^{-2}]$
σ	Fluid electrical conductivity $[S.m^{-\prime}]$
h_f	Heat transfer coefficient $\left[\frac{\mathrm{W}}{\mathrm{m}^2}\mathrm{K}\right]$
K	Permeability of the porous medium $[m^2]$
k_0	Elastic parameter
T	Fluid temperature $[K]$
C	Fluid Concentration $[m\ kg^{-3}]$
k^*	Mean of the absorption coefficient $[m^{-1}]$
σ^*	Sterfan-Boltzmann constant [W · m^{-2} · K^{-4}]
k	Thermal conductivity $[W.m^{-\prime}.K^{-\prime}]$
D	Diffusion coefficient [m^2 $s^{-\prime}$]
μ	Dynamic viscosity $(kgm^{-\prime}s^{-\prime})$

References

[1] Singh, G., Sharma P.R., Chamkha, A.J., 2010. Effect of volumentric heat generation/absorption on mixed convection stagnation point flow on an iso-thermal vertical plate in porous media. *International Journal of Industrial Mathematics*, 2(2), pp.59-71.

[2] Wu, Q., Weinbaum, S., Andreopoulos, Y., 2005. Stagnation point flow in a porous medium. *Chemical Engineering Science,* 60(1), pp.123-134.

[3] Akinbo, B.J., Olajuwon, B.I., 2019. Homotopy analysis investigation of heat and mass transfer flow past a vertical porous medium in the presence of heat source. *International Journal of Heat and Technology*, 37(3), pp. 899-908.

[4] Akinbo, B.J., Olajuwon, B.I., 2019. Convective heat and mass transfer in electrically conducting flow past a vertical plate embedded in a porous medium in the presence of thermal radiation and thermo diffusion. *Computational Thermal Sciences*, 11(4), pp. 367–385.

[5] Akinbo, B.J., Olajuwon, B.I., 2019. Heat and mass transfer in magnetohydrodynamics (MHD) flow over a moving vertical plate with convective boundary condition in the presence of thermal radiation. *Sigma Journal Engineering and Natural Science*, 37(3), pp. 1031-1053.

[6] Ellahi, R., Sait, S.M., Shehzad, N., Ayaz, Z., 2020. A hybrid investigation on numerical and analytical solutions of electro-magnetohydrodynamics flow of nanofluid through porous media with entropy generation. *International Journal of Numerical Methods for Heat and Fluid Flow*, 30(2), pp. 834-854.

[7] Shehzad, N., Zeeshan, A., Ellahi, R., Rashidi, S., 2018. Modelling study on internal energy loss due to entropy generation for non-Darcy Poiseuille flow of silver-water nanofluid: an application of purification. *Entropy*, 20(11), p.851.

[8] Zeeshan, A., Pervaiz, Z., Shehzad, N., Nayak, M.K., Al-Sulami, H.H., 2021. Optimal thermal performance of magneto-nanofluid flow in expanding/contracting channel. *Journal of Thermal Analysis and Calorimetry*, 143, pp.2189-2201

[9] Shehzad, N., Zeeshan, A., Ellahi, R., 2018. Electroosmotic Flow of MHD Power Law Al2O3-PVC Nanofluid in a Horizontal Channel: Couette-Poiseuille Flow Model. *Communications in Theoretical Physics*, 69(6), pp.655-666.

[10] Mahapatra, T.R., Gupta, A.S., 2004. Stagnation-point flow of a viscoelastic fluid towards a stretching surface. *International Journal of Non-Linear Mechanics*, 39, pp.811-820.

[11] Hayat T, Asad S, Mustafa M., Hamed, H. A., 2014. Heat transfer analysis in the flow of Walters' B fluid with a convective boundary condition. Chinese Physics B, 23(8), p.084701.

[12] Hakeem, A.K.A., Ganesh, N.V., and Ganga, B., 2014. Effect of heat radiation in a Walter's liquid B fluid over a stretching sheet with non-uniform heat source/sink and elastic deformation. *Journal of King Saud University - Engineering Sciences*, 26, pp.168-175

[13] Dhanalaxmi, V., 2017. Heat transfer in a viscoelastic fluid over a stretching sheet with frictional heating and work due to deformation. *Global Journal of Pure and Applied Mathematics*, 13(9), pp.6061-6080.

[14] Mishra, S.R., Baag, S., Bhatti, M.M., 2018. Study of heat and mass transfer on MHD Walters B' Nanofluid flow induced by a stretching porous surface. *Alexandria Engineering Journal*, 57, pp.2435–2443.

[15] Qayyum, S., Hayat, T., Shehzad, S.A., and Alsaedi, A., 2017. Effect of a chemical reaction on magnetohydrodynamic (MHD) stagnation point flow of Walters-B nanofluid with newtonian heat and mass conditions. *Nuclear Engineering and Technology*, 49, pp.1636-1644

[16] Hayat, T., Abbas, Z., Pop, I., 2008. Mixed convection in the stagnation point flow adjacent to a vertical surface in a viscoelastic fluid. *International Journal of Heat and Mass Transfer*, 51, pp.3200-3206

[17] Pillai, K.M.C., Sai, K.S., Swamy, N.S., Nataraja, H.R., Tiwari, S.B., Rao, B.N., 2004. Heat transfer in a viscoelastic boundary layer flow through a porous medium. *Computational Mechanics*, 34, pp. 27-37.

[18] Abel, M.S., Mahesha, N., 2008. Heat transfer in MHD viscoelastic fluid over a stretching sheet with variable thermal conductivity, non-uniform heat source and radiation. *Applied Mathematical Modelling*, 32(10), pp.1965-1983.

[19] Abel, M.S., Sanjayanand, E., Nandeppanavar, M. M., 2008. Viscoelastic MHD flow and heat transfer over a stretching sheet with viscous and ohmic dissipations. *Communications in Nonlinear Science and Numerical Simulation*, 13(9), pp.1808-1821.

[20] Abel, M.S., Siddheshwar, P.G., Nandeppanavar, M. M., 2007. Heat transfer in a viscoelastic boundary layer flow over a stretching sheet with viscous dissipation and non-uniform heat source. *International Journal of Heat and Mass Transfer*, 50, pp.960-966.

[21] Cortell R., 2006. Effects of viscous dissipation and work done by deformation on MHD flow and heat transfer of a viscoelastic fluid over a stretching sheet. *Physics Letters A*, 357, pp.298-305.

[22] Makinde, O. D., 2012. Heat and mass transfer by MHD mixed convection stagnation point flow toward a vertical plate embedded in a highly porous medium with radiation and internal heat generation. Meccanica 47, pp. 1173–1184.

[23] Nadeem, S., Mehmood, R., Motsa, S.S., 2003. Numerical investigation on MHD oblique flow of Walter's B type nanofluid over a convective surface. *International Journal of Thermal Sciences* 92, pp. 162-172

[24] Zeeshan, A., Shehzad, N., Ellahi, R., 2018. Analysis of activation energy in Couette-Poiseuille flow of nanofluid in the presence of chemical reaction and convective boundary conditions. *Results in Physics*, 8, pp.502-512.

[25] Alamri, S. Z., Ellahi, R., Shehzad, N., Zeeshan, A., 2019. Convective radiative plane Poiseuille flow of nanofluid through porous medium with slip: An application of Stefan blowing. *Journal of Molecular Liquids*, 273, pp.292-304

[26] Liao S. J., 2003. Beyond perturbation: an introduction to Homotopy Analysis Method. Boca Raton, Fla., USA: *Chapman and Hall.*

[27] Akinbo, B.J., Olajuwon, B.I., 2021. Radiation and thermal-diffusion interaction on stagnation-point ow of Walters' B uid toward a vertical stretching sheet. *International Communications in Heat and Mass Transfer*, 126, pp.105471

[28] Akinbo, B.J., Olajuwon, B.I., 2021. Heat transfer analysis in a hydromagnetic Walters' B uid with elastic deformation and Newtonian heating. *Heat Transfer*, 50, pp.2033-2048.

[29] Shahid, A., Bhatti, M.M., Bég, O.A., Kadir, A., 2018. Numerical study of radiative Maxwell viscoelastic magnetized flow from a stretching permeable sheet with the Cattaneo–Christov heat flux model. *Neural Computing and Applications*, 30(11), pp.3467-3478.